Correlating elemental distribution with mechanical properties of TiN/SiNx nanocomposite coatings

M. Sperr [a], Z.L. Zhang [b], Y.P. Ivanov [b], P.H. Mayrhofer [a], M. Bartosik [a,*]

[a] Institute of Materials Science and Technology, TU Wien, A-1060 Vienna, Austria
[b] Erich Schmid Institute of Materials Science, Austrian Academy of Sciences, A-8700 Leoben, Austria

ARTICLE INFO

ABSTRACT

Detailed structural and chemical analyses reveal that Ti-Si-N coatings prepared with high nitrogen partial pressure and temperature are composed of nm-sized (nearly equiaxed) TiN crystallites encapsulated by ~1.0 nm thin Si-rich tissue phase. This nanocomposite structure allows for superior hardness (37.6 ± 1.5 GPa) and fracture toughness (4.5 ± 0.6 MPa√m). Contrary, deposition at lower nitrogen partial pressure and temperature does not allow for such a clear Si segregation during film growth, leading to nm-sized solid solution $Ti_{1-x}Si_xN$ crystallites. Although having the same Si content of 8.5 at.%, their hardness (32.1 ± 0.9 GPa) as well as fracture toughness (3.0 ± 0.2 MPa√m) is significantly lower.

Nanocomposite nitride coatings rank among the hardest materials known. The high hardness is based on the small grain size preventing the formation and propagation of flaws (such as dislocations) and strong interfacial layers hindering grain boundary sliding [1]. A typical representative of such a nanocomposite material is TiN-SiNx, characterized by a self-organized structure composed of TiN nanocrystals percolated by a silicon nitride (SiNx) tissue phase [2]. Theoretical studies in the framework of density functional theory found that the strength of TiN-SiNx reaches a maximum when the SiNx interfacial material is only one monolayer thin. The strengthening effect is based on valence charge transfer from the TiN nanocrystals to the tissue phase [3]. If the thickness of SiNx exceeds one monolayer, too much valence charge density will be transferred from TiN to SiNx, which results in weakening of the Ti—N bonds in the TiN nanocrystals close to the SiNx interface (and hence the Ti—N bonds become the weak links).

The atomic structure of the SiNx interfacial material has been widely debated. While silicon nitride exists in several polymorphs (the most common ones are hexagonal β-Si₃N₄, α-Si₃N₄, and spinel-type γ-Si₃N₄), Fallqvist et al. [4] have shown recently using atomically resolved electron microscopy methods that metastable SiNx assumes the structure of the adjacent TiN, i.e., the face-centred cubic (B1) structure, in epitaxial TiN/SiNx nanolayers. Similar findings have been reported in earlier studies (e.g., [5,6]).

The goal of the present work is to compare the mechanical properties of Ti-Si-N nanocomposite films having clearly separated phases (TiN nanocrystals encapsulated by a thin Si-rich tissue phase) with those having a more gradient transition between solid solution $Ti_{1-x}Si_xN$ nanocrystals and tissue phase. The different nanostructures are realized by adapting the film deposition conditions (basically substrate temperature and nitrogen partial pressure) and their elemental distribution is studied by various techniques including electron energy loss spectroscopy (EELS). In particular, we show how the nanostructure characteristics influence the fracture toughness by conducting state-of-the-art microcantilever bending experiments on free-standing film material.

The resulting nanostructure of Ti-Si-N materials strongly depends on the underlying formation principles during preparation by magnetron sputtering, see for example Refs. [7,8]. Roughly, the process can be seen as a sort of decomposition of the randomly arriving atoms at the surface. To provide the required driving force for phase separation of Ti-Si-N towards TiN and SiNx, a sufficiently high nitrogen pressure is needed, which is about 2×10^{-3} mbar [7] during reactive magnetron sputtering. As this phase separation is diffusion-driven, also the deposition temperature needs to be sufficiently high to be completed during deposition, for example >550 °C as reported in [7]. Of course, this strongly depends on the growth rate itself. If these conditions are met, only the strain energy connected with the phase separation could hinder the decomposition. However, for Ti-Si-N, the energy-gain by de-mixing is significantly larger than the connected energy-cost. Besides the mentioned substrate temperature and nitrogen partial

* Corresponding author.
E-mail address: matthias.bartosik@tuwien.ac (M. Bartosik).

pressure, a low concentration of oxygen impurities is required to achieve good mechanical properties, see for instance Ref. [9].

The coatings of the present study were deposited on Si (100) substrates ($20 \times 7 \times 0.5$ mm^3) in an AJA Orion 5 reactive magnetron sputter system. By dc powering one 3″ TiSi$_2$-alloyed Ti target (having an overall Si content of 15 at.%, Plansee Composite Materials GmbH), we obtained coatings with an overall Si content of ~8.5 at.%. We carried out several depositions with different N$_2$/Ar flow ratios (f), deposition temperatures (T_{dep}), and target power densities. The hardest coatings were prepared with $f > 1$ and T_{dep} between 500 and 700 °C. Here, we will show the results for our hardest coating, ~2.6 μm thick (deposition rate ~87 nm/min), prepared with $f = 6/4$ (total pressure of 0.4 Pa), target power density of ~22 W/cm^2, and $T_{dep} = 700$ °C. The low base pressure of $<5 \cdot 10^{-7}$ mbar at room temperature before the deposition ensured for a low oxygen content. This coating is compared with a film grown with a lower f of 3/7 and a lower T_{dep} of 500 °C, presented already in an earlier study [10].

The structure of the films was studied by X-ray diffraction (XRD) using a PANalytical Empyrean diffractometer (Cu-Kα radiation) in symmetric Bragg Brentano geometry. The lattice constants of our coatings were determined from θ-2θ scans of the 220 peaks acquired at the strain-free tilt angle ψ^*, defined as [11]:

$$\sin^2\psi^*(hkl) = \frac{-2s_1(hkl)}{\frac{1}{2}s_2(hkl)} \tag{1}$$

The X-ray elastic constants $s_1(hkl)$ and $\frac{1}{2}s_2(hkl)$ were calculated using single crystal elastic constants of TiN from Density Functional Theory simulations [12] and applying the Hill grain interaction model [13] resulting in $\psi^*(220) \sim 40°$. The local elemental distribution with atomic-scale spatial resolution was studied with transmission electron microscopy. EELS experiments were performed at the Titan 60–300 TEM (FEI Company) at 300 kV with a post-column EEL spectrometer (Quantum GIF Gatan). The optical conditions of the microscope for the STEM EELS spectrum-image were set to obtain a probe-size of 0.14 nm, with a convergence semi-angle of 10 mrad and collection semi-angle of 12 mrad. The dispersion was set to 0.25 eV per channel and the estimated energy resolution was about 1.5 eV using the zero-loss spectrum. The hardness was determined using a Fischer Cripps Laboratories ultra-micro indentation system (UMIS) equipped with a Berkovich tip; 30 indents per sample with increasing maximum loads from 3 to 45 mN were made. The influence of the substrate material on the hardness values was minimized by considering only indents with indentation depths below 10%. The data were evaluated according to Oliver and Pharr [14].

The fracture toughness was obtained by state-of-the-art micro-cantilever bending tests [15] of free-standing film material. The cantilevers with dimensions of ~t × t × 7 * t (t: film thickness) were focused ion beam machined from the film material using 1 nA (30 kV) for coarse cuts, 500 pA (30 kV) for final polishing, and 50 pA (30 kV) for machining the pre-notch. The cantilevers were loaded until failure inside a scanning electron microscope (FEI Quanta 200 FEGSEM) equipped with a PI85 PicoIndenter (Hysitron) using a spherical diamond tip (tip radius of ~1 μm). The recorded load-displacement data (not shown) suggest that all tested coatings deformed in a linear elastic manner until failure. Hence, we used linear elastic fracture mechanics according to Ref. [16] to determine the critical stress intensity factors from the maximum loads at failure. The actual cantilever dimensions and the pre-notch lengths were obtained post-mortem from the fractured cross sections.

XRD investigations (Fig. 1) reveal a face-centered cubic (fcc) structure for both Ti-Si-N coatings. However, the coating prepared with higher f and T_{dep} exhibits major XRD peaks with predominant Lorentzian shape, indicative for almost defect-free nanocrystals [17]. Contrary, the peak shape of the XRD peaks from the film prepared with lower f and T_{dep} can be best described by a Gaussian function, indicative for microstrains [17]. This could evince the substitution of Ti by Si. The lattice
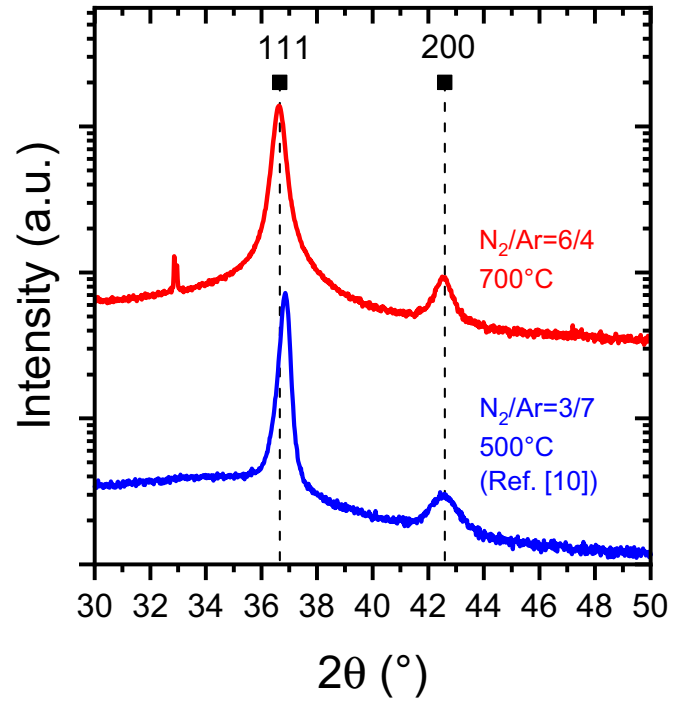

Fig. 1. X-ray diffraction θ-2θ scans of TiN-SiN$_x$ films grown with different nitrogen partial pressures and substrate temperatures acquired at $\psi = 0°$ showing fcc 111 and 200 reflections. The peak positions marked in the diagram correspond to TiN according to the JCPDF database file card #38-1420. (The sharp peak in the red XRD pattern at ~33° stems from the Si substrate).

distortion due to the different atomic radii of Si and Ti and/or due to other point and line defects within the crystalline phase results in slight variations of the d-spacing. Therewith associated slight variations of the scattering angles lead to broadening of the Bragg peaks (Gaussian strain broadening) [18]. Although TiN and SiN$_x$ are immiscible under equilibrium conditions [7], the driving force for phase separation of Ti-Si-N towards TiN and SiN$_x$ is low for low f and/or completion of the diffusion-driven segregation process is prevented at low T_{dep} in the film growth process. Hence, such growth conditions far from equilibrium allow substitution of Ti by Si.

Experimental studies as well as theoretical calculations based on density functional theory calculations clearly showed that the lattice parameter of solid solution fcc-Ti$_{1-x}$Si$_x$N, $a_0(x)$, decreases monotonically with increasing Si content x with da$_0$/dx ~ − 0.0018 Å/at% Ti-substitute [19]. The lattice constants of our two coatings are 4.23 and 4.22 Å when prepared with higher or lower f and T_{dep}, respectively. The 0.01 Å smaller lattice parameter of the coatings prepared with low f and T_{dep} implies that there, a larger share of Si atoms (according to da$_0$/dx ~ − 0.0018 Å/at% and Ref. [19] about 6 at%) substitutes for Ti within the TiN crystals to form an fcc-Ti$_{1-x}$Si$_x$N solid solution.

The other sample is investigated in detail by TEM. Fig. 2 presents a series of images taken from plan-view samples. The low-magnification high-angle annular dark-field (HAADF) image (Fig. 2a) shows a very homogeneous morphology with a random orientation of nearly equiaxed nanocrystals of sizes between 10 and 20 nm. The medium-magnification HAADF image (Fig. 2b) indicates the presence of low-density tissue phases percolating through the entire cross section. Here, thinner and thicker dark-contrast regions can be identified. This is highlighted in the higher magnification HAADF image (Fig. 2c). Fig. 2d represents an EELS elemental map acquired from this grain boundary and triple junction region marked in Fig. 2c. This explicitly shows a high fraction of Si at grain boundaries and triple junctions, indicating that for this deposition condition, Si is rather resided there forming likely a SiN$_x$ tissue than substituting for Ti in the nanocrystals (as already suggested by the

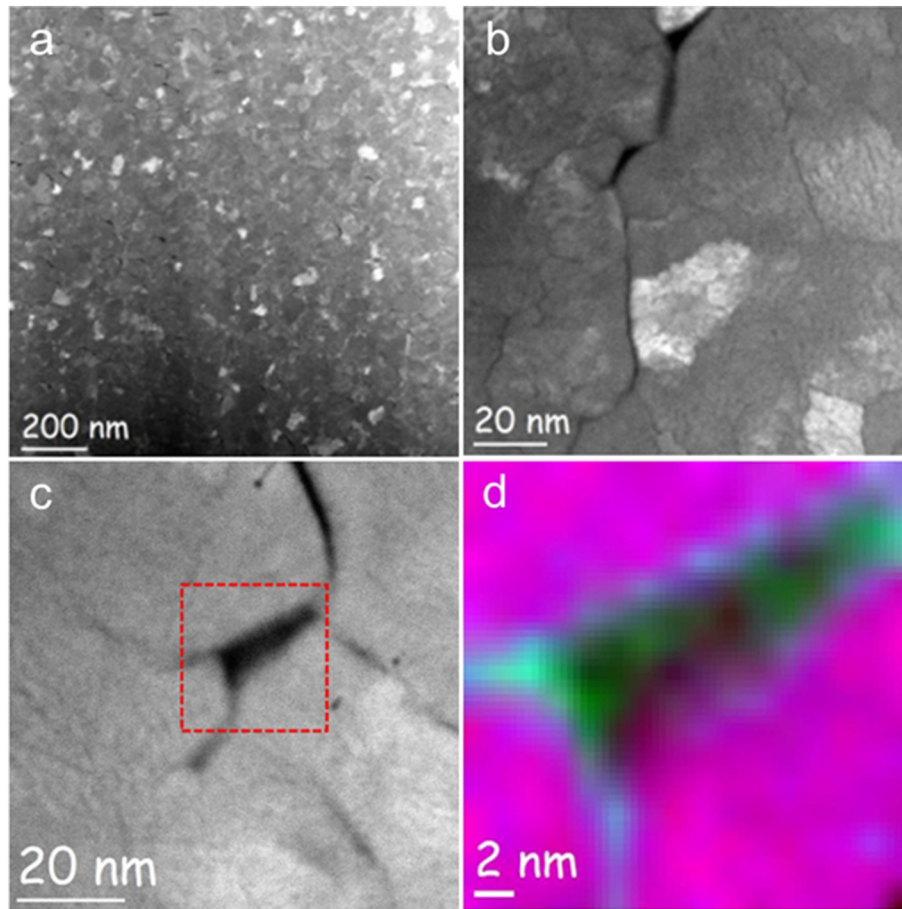**Fig. 2.** Plan-view STEM images of the TiN/SiN$_x$ nanocomposite prepared with high f and T_{dep}. (a) Low-magnification HAADF image, (b) medium-magnification HAADF image, (c) high-magnification HAADF image. The area used for chemical analysis is marked with a red-dashed square. The corresponding EELS map obtained using Si_L$_{2,3}$, N_K and Ti_L$_{2,3}$ absorption edges (d) clearly indicates that Si segregates to grain boundaries and triple junctions (green: Si, blue: N, red: Ti).

XRD investigations and the obtained lattice parameter). The SiN$_x$ tissue phase is ~1.0 nm thin, in agreement with HRTEM investigations, Fig. 3. These investigations furthermore show that the nanocrystalline phase is basically TiN. As mentioned above, the thickness of the Si-rich tissue
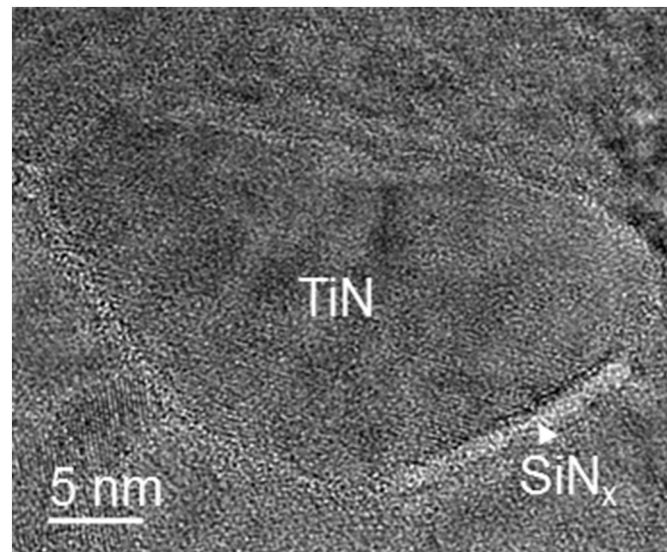

Fig. 3. Representative plan-view HRTEM image showing a TiN nanocrystallite encapsulated by ~1-nm-thin SiN$_x$ tissue phase.

phase encapsulating the TiN nanocrystals is not fully homogeneous, but differs slightly.

The nc-TiN/SiN$_x$ nanocomposite with an almost complete separation into fcc-TiN and SiN$_x$ tissue phase prepared with a high f and T_{dep} exhibits a remarkably higher hardness (H) of 37.6 $\pm$ 1.5 GPa than its chemically comparable counterpart (H = 32.1 $\pm$ 0.9 GPa [10]). Furthermore, also the obtained fracture toughness is with 4.5 $\pm$ 0.6 MPa$\sqrt{m}$ significantly higher when guaranteeing for an almost complete percolation and phase separation into nc-TiN and a thin SiN$_x$ tissue phase. The coating prepared with lower f and T_{dep} exhibits 3.0 $\pm$ 0.2 MPa$\sqrt{m}$ for a comparable overall chemical composition [10]. This comparison is also presented in Fig. 4a and b, respectively, where we also added the Si-dependent H and K$_{IC}$ values of the coatings prepared with lower f and T_{dep} reported in Ref. [10].

The higher hardness and K$_{IC}$ value for the Ti-Si-N coating with nc-TiN crystals encapsulated by a thin SiN$_x$ tissue phase agree with Density Functional Theory calculations, predicting the highest cohesive strength if TiN nanocrystals are covered by one monolayer SiN$_x$ [3]. Although the theoretical strength of SiN$_x$ is lower than that of defect-free TiN, it improves considerably the cohesive strength of the grain and phase boundaries, which can be seen as the weak link in these coatings. For example, the fracture toughness of a TiN coating itself is only 1.9 $\pm$ 0.4 MPa$\sqrt{m}$ [10]. Also this value can be increased to 2.6 $\pm$ 0.3 MPa$\sqrt{m}$ [20] when optimizing the deposition conditions and hence altering the film microstructure (cf. Ref. [21]). However, the TiN/SiN$_x$ nanocomposite still clearly outperforms TiN and other reactively magnetron sputtered coatings like Ti$_{0.4}$Al$_{0.6}$N (2.7 $\pm$ 0.3 MPa$\sqrt{m}$ [22]) and TiN/CrN superlattices (2.0 $\pm$ 0.2 MPa$\sqrt{m}$ [23]), and even rivals the peak fracture
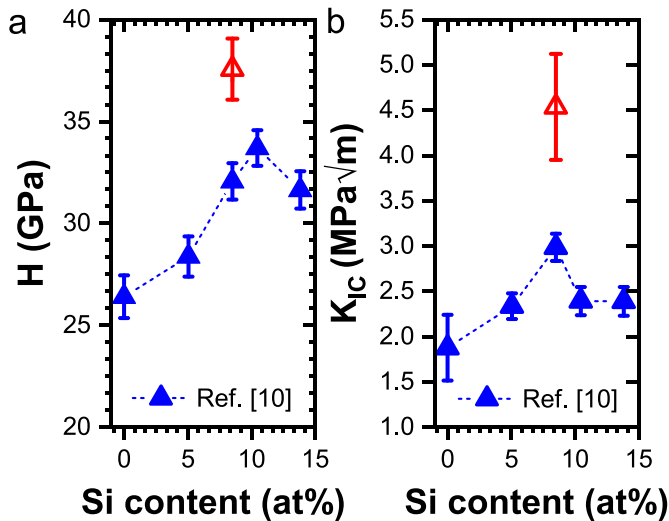
Fig. 4. Si-dependent hardness (a) and fracture toughness (b) values of Ti-Si-N films (blue data points from Ref. [10]). When using higher f and T_{dep} in the deposition process, Si segregates to the grain boundaries and forms a ~1.0 nm thin SiN_x interfacial phase encapsulating TiN nanocrystals, which leads to enhanced mechanical properties (red data points).

toughness recorded for epitaxial TiN/WN superlattices grown on MgO (100) platelets (4.6 ± 0.2 MPa√m [24]).

Finally, nanocomposite coatings possess a very high resistance against failure, which is not necessarily based on high fracture toughness, but on the small size of flaws in such materials (on the order of 1–2 nm) [2,25]. As a consequence of the essentially flaw-free TiN nanocrystals, crack initiation and propagation within the nm-thin interfacial SiN_x component is the most probable fracture mechanism (i.e., inter-granular failure). Considering the stress intensity factor $K_1 = \sigma \sqrt{\pi * a_{crack}}$, it is obvious that for small nanocracks (a_{crack} = a few nm) in nanocomposites, an order of magnitude higher stress σ has to be applied to induce their propagation as compared with a fine grained ceramic ($a_{crack} = 100 - 200$ nm), even if the stress intensity would be the same (cf. [2,25]).

To conclude, the strengthened interfaces and the small and sparse flaws enable not only a high hardness but also a high resistance against failure when the nanocomposite coatings are synthesized under appropriate deposition conditions. Full segregation of Si to the grain boundaries forming a thin SiN_x tissue phase with a sharp interface to the TiN nanocrystallites is crucial for achieving a high performance in terms of the mechanical properties.

References

[1] V. Kanyanta (Ed.), Microstructure-Property Correlations for Hard, Superhard, and Ultrahard Materials, Springer International Publishing, Switzerland, 2016.
[2] S. Veprek, A.S. Argon, J. Vac. Sci. Technol. B 20 (2002) 650.
[3] R.F. Zhang, A.S. Argon, S. Veprek, Phys. Rev. B 81 (2010), 245418.
[4] A. Fallqvist, W. Olovsson, B. Alling, J. Palisaitis, M.P. Belov, I.A. Abrikosov, L. Hultman, P.O.Å. Persson, Phys. Rev. Mater. 2 (2018), 093608.
[5] H. Söderberg, M. Odén, T. Larsson, L. Hultman, J.M. Molina-Aldareguia, Appl. Phys. Lett. 88 (2006), 191902.
[6] L. Hultman, J. Bareño, A. Flink, H. Söderberg, K. Larsson, V. Petrova, M. Odén, J.E. Greene, I. Petrov, Phys. Rev. B 75 (2007), 155437.
[7] R.F. Zhang, S. Veprek, Mater. Sci. Eng. A 424 (2006) 128.
[8] J. Patscheider, MRS Bull. 28 (2003) 180.
[9] S. Veprek, P. Karvankova, M.G.J. Veprek-Heijman, J. Vac. Sci. Technol. B 23 (2005) L17.
[10] M. Bartosik, R. Hahn, Z.L. Zhang, I. Ivanov, M. Arndt, P. Polcik, P.H. Mayrhofer, Int. J. Refract. Met. Hard Mater. 72 (2018) 78.
[11] M. Bartosik, R. Daniel, C. Mitterer, I. Matko, M. Burghammer, P.H. Mayrhofer, J. Keckes, Thin Solid Films 542 (2013) 1.
[12] F. Tasnádi, I.A. Abrikosov, L. Rogström, J. Almer, M.P. Johansson, M. Odén, Appl. Phys. Lett. 97 (2010), 231902.
[13] I.C. Noyan, J.B. Cohen, Residual Stress: Measurement by Diffraction and Interpretation, Springer, Berlin, 1987.
[14] W.C. Oliver, G.M. Pharr, J. Mater. Res. 7 (1992) 1564.
[15] G. Dehm, B.N. Jaya, R. Raghavan, C. Kirchlechner, Acta Mater. 142 (2018) 248.
[16] K. Matoy, H. Schönherr, T. Detzel, T. Schöberl, R. Pippan, C. Motz, G. Dehm, Thin Solid Films 518 (2009) 247.
[17] R.L. Snyder, J. Fiala, H.J. Bunge, Defect and Microstructure Analysis by Diffraction, Oxford University Press Inc, New York, 1999.
[18] C.E. Krill, R. Haberkorn, R. Birringer, in: H.S. Nalwa (Ed.), Handbook of Nanostructured Materials and Nanotechnology, vol. 2, Academic Press, San Diego 2000, pp. 155–211 , Spectroscopy and Theory.
[19] G. Greczynski, J. Patscheider, J. Lu, B. Alling, A. Ektarawong, J. Jensen, I. Petrov, J.E. Greene, L. Hultman, Surf. Coat. Technol. 280 (2015) 174.
[20] T. Grünstäudl, Comparative Fracture Toughness Analysis of Hard Coatings by In-situ Microcantilever and Cube-Corner Experiments, Diploma Thesis, 2017.
[21] Z. Xu, Z. Zhang, M. Bartosik, Y. Zhang, P.H. Mayrhofer, Y. He, J. Alloys Compd. 754 (2018) 257.
[22] M. Bartosik, C. Rumeau, R. Hahn, Z.L. Zhang, P.H. Mayrhofer, Sci. Rep. 7 (2017), 16476.
[23] R. Hahn, M. Bartosik, R. Soler, C. Kirchlechner, G. Dehm, P.H. Mayrhofer, Scr. Mater. 124 (2016) 67.
[24] J. Buchinger, N. Koutná, Z. Chen, Z. Zhang, P.H. Mayrhofer, D. Holec, M. Bartosik, Acta Mater. 172 (2019) 18.
[25] S. Veprek, Rev. Adv. Mater. Sci. 5 (2003) 6.